

<https://doi.org/10.1038/s43247-024-01307-9>

Synoptic and planetary-scale dynamics modulate Antarctic atmospheric river precipitation intensity

Check for updates

Rebecca Baiman¹ ✉, Andrew C. Winters¹, Benjamin Pohl², Vincent Favier³, Jonathan D. Wille^{3,4} & Kyle R. Clem⁵

Although rare, atmospheric rivers substantially influence the interannual variability of Antarctic surface mass balance. Here we use MERRA-2 reanalysis to identify characteristics unique to atmospheric river environments by comparing (1) Analog (environments that feature high-low pressure couplets, similar to Atmospheric River environments, but no Atmospheric River), (2) Atmospheric River, and (3) Top Atmospheric River (highest precipitation) timesteps during 1980–2019 around Antarctica. We find significant differences between Atmospheric River and Analog environments including more intense and poleward-shifted mid-tropospheric geopotential height couplets as well as larger atmospheric moisture anomalies. We find similar significant enhancement in synoptic-scale dynamic drivers of Top Atmospheric Rivers compared to all Atmospheric River environments, but no significant difference in local integrated water vapor anomalies. Instead, our results highlight the importance of large-scale dynamic drivers during Top Atmospheric River timesteps, including amplified Rossby waves excited by tropical convection.

Precipitation is the dominant source of mass for the Antarctic Ice Sheet (AIS)¹ and, despite some estimates that Atmospheric Rivers (ARs) only occur ~3 days per year at any location, ARs control the interannual variability of precipitation across most of Antarctica². ARs are narrow filaments of enhanced water vapor transport that result in generally intense precipitation over the AIS via orographic lift or vertical motion associated with the warm conveyor belt of an attendant extratropical cyclone^{3–5}. AR impacts include both negative and positive contributions to the AIS mass balance. In particular, ARs advect warm, moist air masses from lower latitudes towards the continent, increasing cloud-liquid water content, and thus downward longwave radiation. The resulting warmer surface temperatures can cause surface melt^{6–10}, while concurrent sea-ice melt¹¹ and large ocean swells from AR activity can contribute to ice shelf instability and trigger calving events if sea ice is dispersed^{2,12}. Wille et al.¹³ finds that ARs catalyzed 60% of Antarctic Peninsula calving events between 2000 and 2020, concluding that short term atmospheric events including ARs play a role in ice shelf stability. Despite these negative contributions to AIS mass balance, and their potential to increase in importance as the climate warms, snowfall dominates Antarctic

AR impacts in the current climate^{2,14}, with one study estimating that ARs explain $13\% \pm 3\%$ of total AIS precipitation per year between 1980–2020¹⁴. The AR impacts during 2022 further illustrate the significance of these events, with AR related precipitation contributing to a rare net mass gain in Antarctica, overwhelming the ocean-driven mass loss in the Amundsen Sea Embayment¹⁵.

The importance of ARs to the AIS mass balance, and thus global sea levels, motivates a deeper understanding of the atmospheric environments most conducive to landfalling Antarctic ARs. Regional and individual case studies associate Antarctic ARs with an amplified mid-troposphere geopotential height pattern as well as a surface high-low pressure couplet^{6,12,16,17} over the Southern Ocean which acts to transport moisture poleward ahead of a cyclone's attendant cold front. However, not all pressure couplets result in ARs¹⁶, prompting the question of what makes AR environments unique? We respond with a *circumpolar* Antarctic AR study investigating environmental features unique to Antarctic AR environments relative to other high-amplitude atmospheric flow patterns over the Southern Ocean. Using MERRA-2 reanalysis data¹⁸ between 1980–2019, as well as a polar-specific

¹Department of Atmospheric and Oceanic Sciences, University of Colorado Boulder, Boulder, CO, USA. ²Biogéosciences, CNRS / Université de Bourgogne Franche-Comté, Dijon, France. ³Institut des Géosciences de l'Environnement, CNRS/UGA/IRD/G-INP, Saint Martin d'Hères, France. ⁴Institute for Atmospheric and Climate Science, ETH Zurich, Zurich, Switzerland. ⁵School of Geography, Environment and Earth Sciences, Victoria University of Wellington, Wellington, New Zealand. ✉e-mail: rebecca.baiman@colorado.edu

AR detection algorithm¹⁰, we define and compare three collections: (1) landfalling Antarctic AR timesteps, (2) Analog timesteps: synoptic-scale environments that are most similar to each AR timestep but do not feature an AR, and (3) Top AR timesteps: the top 10% of AR timesteps with respect to snowfall intensity on the AIS and ice shelves (see methods).

Comparing AR timesteps to the associated Analog collection, we find that ARs feature an anomalous geopotential height and attendant surface pressure couplet that facilitates warm-air advection and induces more precipitation over the Antarctic continent. The subset of Top AR timesteps reveal regionally dependent planetary-scale dynamics, such as interactions between midlatitude Rossby waves and those excited by tropical convection, that result in more amplified mid-tropospheric geopotential height and surface pressure couplets relative to all AR timesteps. However, Top AR timesteps do not feature meaningful differences in local vertically integrated moisture anomalies relative to all AR timesteps. We conclude that although Antarctic ARs rely on both ample moisture and lift to produce precipitation, lift plays a more important role than vertically integrated moisture availability in driving the highest intensity AR precipitation. The unique environments and atmospheric drivers of AR precipitation identified in this study contribute to a growing field of research on AR impacts to the AIS in the current climate. Subsequent research can leverage this perspective to investigate increasingly complex Antarctic AR impacts in a future climate.

Results

AR impacts and defining a “Top AR” category

We begin by considering the dominant impact of ARs on the AIS: a comparison of snowfall intensity over the ice sheet and ice shelves associated with AR and Analog timesteps. Note that each Analog timestep is chosen at the same location as an AR timestep so the distributions of AR and Analog timesteps by longitude are identical (See “Methods” for detailed description). As expected, AR timesteps feature significantly higher snowfall accumulations (Fig. 1a), with the mean and median snowfall intensity of AR timesteps ranking higher than 95% of Analog timesteps. In addition to pinpointing features of AR environments that are distinct from Analog environments, we hope to identify characteristics that separate high-impact AR environments from the full collection of AR timesteps. We choose snowfall intensity to define high-impact AR timesteps because snowfall is the primary impact from ARs to the surface mass balance (SMB) in the current climate^{2,14}. We define the subset of AR timesteps that rank in the top 10% of AR snowfall intensity as “Top ARs”. The Top AR timesteps are associated with higher snowfall intensity than 99% of Analog timesteps (Fig. 1a).

The following results compare the synoptic-scale environments between three groups: (1) 17,418 landfalling Antarctic AR timesteps across our study period, (2) a corresponding group of 17,418 Analog timesteps that feature the closest matching synoptic-scale environment to each AR timestep but are not associated with an AR, and (3) 1742 Top AR timesteps, the

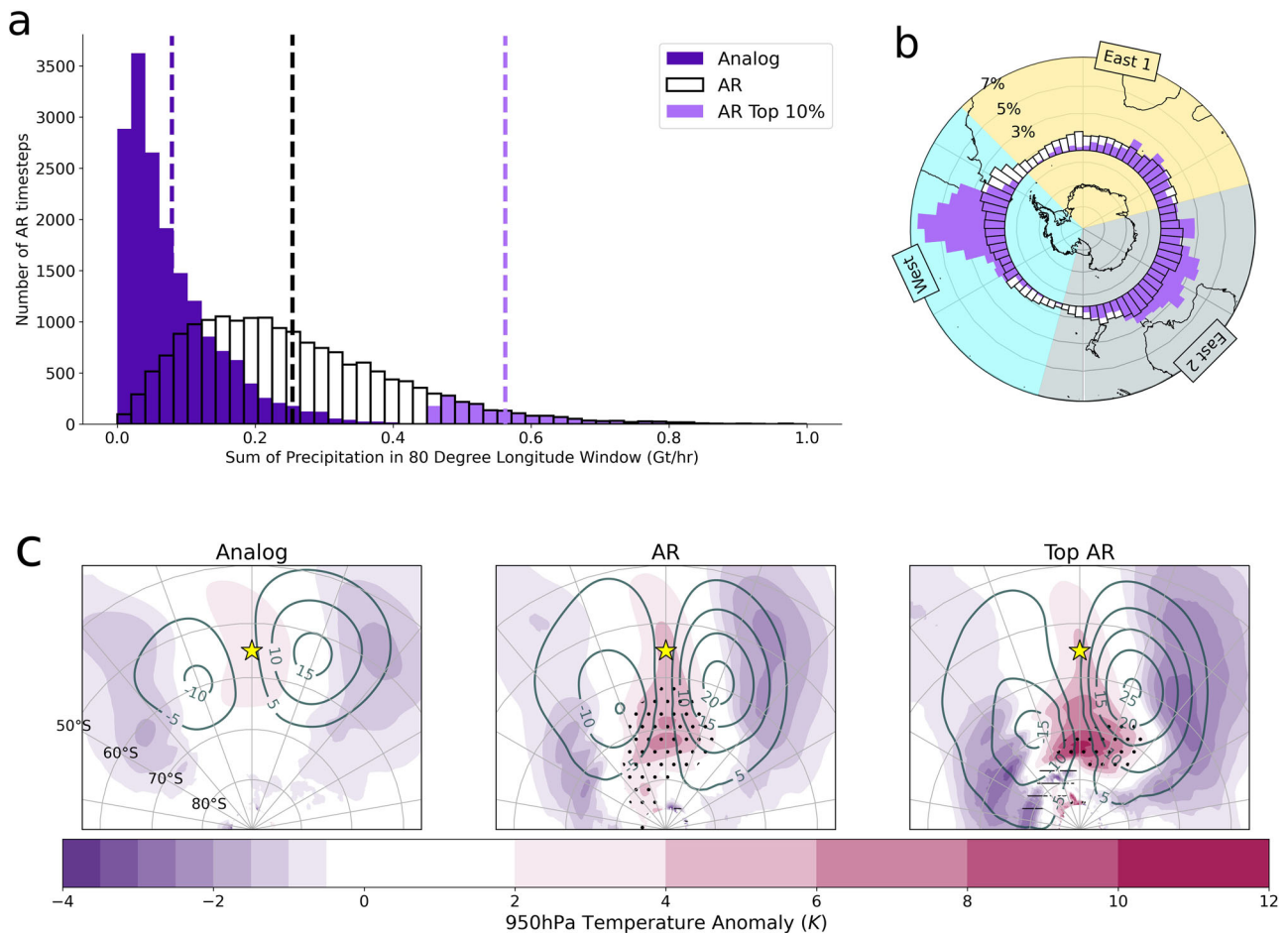


Fig. 1 | AR Impacts. a Distributions of snowfall intensity over the Antarctic Ice Sheet and ice shelves during Analog (dark purple), AR (clear), and Top AR (light purple) timesteps. Mean values for each group are shown with dashed lines. **b** Longitudinal distributions of AR centers at 55°S for AR (clear) and Top ARs (light purple) expressed as a percentage of all timesteps within each respective group. Three regional sectors are shaded and labeled: West (light blue), East 1 (yellow), and East 2

(gray). **c** Composites of 950hPa temperature anomalies (shading) and SLP anomalies (dark green contours in hPa) from 90°S to 40°S for Analog, AR, and Top AR timesteps centered on the AR center at 55°S (yellow star). Stippling (hatching) indicates statistically significantly higher (lower) temperature anomalies in the AR composite relative to the Analog group, or in the Top AR group relative to the AR group at grid points where the difference in composite anomalies are greater than 1 K.

top 10% of all AR timesteps with respect to snowfall intensity. See the Methods section for a detailed description of how each category is defined as well as the appropriate statistical significance tests applied to each category.

Note that our choice of selecting Top ARs based on snowfall intensity differs from previous literature that defines extreme ARs based on integrated vapor transport (IVT) or integrated water vapor (IWV)^{13,19}. Timesteps within our Top AR category only overlap with 9.8% (10%) of the AR timesteps that rank in the top 10% of AR maximum IWV (IVT). Thus our Top AR subset is distinct from a categorization based on maximum IVT or IWV and is a unique grouping of high-impact AR timesteps.

An initial investigation of the spatial variability of all ARs shows a relatively smooth circumpolar distribution of AR centers at 55°S (Fig. 1b). We further divide ARs into three regions by longitude (see Methods), and find that 33% occur in the West sector, 32% in East 1, and 35% in East 2. Unlike ARs, Top ARs demonstrate a strong preference for certain regions, with 45% occurring in the West sector, 16% in East 1, and 39% in East 2 (Fig. 1b). Similarly, we find that ARs are distributed relatively evenly throughout the seasons (22% in DJF, 25% in MAM, 27% in JJA, 26% in SON), whereas Top ARs are more common in austral fall and winter (12% in DJF, 32% in MAM, 33% in JJA, 23% in SON).

In addition to precipitation, ARs can impact SMB of the AIS via surface melting induced by the advection of moist, warmer air masses from lower latitudes as well as increased downward longwave radiation from liquid-laden cloud cover that accompanies ARs^{10,20,21}. We explore anomalous near-surface temperatures in Fig. 1c and find that AR environments result in significantly higher temperature anomalies compared to Analog timesteps, particularly near the Antarctic coast (66–75°S). Compared to all ARs, Top AR environments feature significantly higher near-surface temperatures along the coast, indicating that Top AR timesteps are associated with larger temperature anomalies and thus a greater potential for surface melt compared to all ARs.

Synoptic-scale dynamics of AR environments

Motivated by the significant differences in impacts associated with Analog, AR, and Top AR environments noted in the previous section, we investigate the synoptic-scale dynamics potentially driving those differences. 500-hPa geopotential height (H500) anomaly composites associated with Analog, AR, and Top AR timesteps (Fig. 2a) demonstrate that all three categories feature an anomalous H500 couplet, consistent with previous findings^{2,16,22}. Despite selecting Analog timesteps that best-match the AR H500 anomalies at 55°S, the H500 anomaly couplet associated with AR timesteps is stronger, shifted poleward, and meridionally elongated compared to the Analog composite. The Top AR composite is similarly enhanced relative to the AR composite, exhibiting stronger H500 anomalies near the Antarctic coast (Fig. 2a). We note that Analog, AR, and Top AR composites also feature strong sea-level pressure (SLP) couplets that are located east of their counterpart mid-troposphere height anomaly couplet (Fig. 2a, c). This westward vertical tilt with height is conducive to intensification of the surface pressure anomalies. The SLP couplets in the AR and Top AR environments are also larger in magnitude and shifted poleward compared to the Analog environment.

Investigating the change in mid-troposphere geopotential heights from 24 h before AR landfall to 24 h after landfall, we observe a poleward elongation of the mid-tropospheric ridge during AR events that is not observed during Analog events (Fig. 2b). This elongation could be attributed to the effects of latent heating in conjunction with warm air advection and other dry baroclinic processes that act to strengthen the mid-tropospheric ridge in the vicinity of the AR^{21,16,23}. Consistent with this hypothesis, the poleward shift and meridional elongation of the mid-tropospheric ridge are further exaggerated in the Top AR composite compared to the full AR group, where stronger diabatic processes accompany the production of heavier precipitation (e.g. compare the position of the +75hPa contour in the AR and Top AR composites; Fig. 2b).

The enhanced mid-tropospheric waviness in AR timesteps and the Top AR subset (Fig. 2a) directly translates to intensified surface pressure

couplets (Fig. 2c) via the presence of larger upper-level divergence in areas of stronger flow curvature. Intensified cyclones in the AR and Top AR composites are subsequently capable of stronger vertical motion in the vicinity of the AR via their associated warm conveyor belts. Furthermore, the stronger poleward geostrophic flow in the AR and Top AR composites enhances orographic lift, which contributes to the elevated levels of vertical motion near the coast in those composites (stippling south of 60°S in Fig. 2c)^{3,4,17,24}. These intensified dynamics associated with AR and Top AR environments are also consistent with increased AIS impacts: stronger poleward geostrophic flow results in larger temperature anomalies (Fig. 1c) and increased vertical motion enhances precipitation (Fig. 1a). We note that the aforementioned characteristics are significantly enhanced in the AR versus Analog composites as well as in the Top AR subset versus the AR composite.

Moisture in AR environments

Current AR literature often defines AR intensity globally using IWV or meridional integrated vapor transport (vIVT)^{13,19}, relying on the moisture availability or moisture transport within the AR as a predictor for resultant AR impacts²⁵. To explore the relationship between moisture availability, moisture transport, and snowfall intensity we plot AR-centered composites of IWV and vIVT for Analog, AR, and Top AR timesteps in Fig. 3a, b. We find that AR timesteps have significantly more IWV and vIVT compared to Analog timesteps. This is an expected result given (1) the Wille et al. AR detection algorithm¹⁰ used in this study includes a relatively high threshold for anomalous vIVT as a requirement for AR detection²⁶ and (2) our physical understanding that ARs feature elevated moisture⁵. We observe spatially that areas of anomalous IWV and vIVT for the AR timesteps are elongated meridionally and shifted poleward compared to their Analog counterparts, reflecting the differences in mid troposphere and surface dynamics shown in Fig. 2a, c. When we compare the Top AR subset against all AR timesteps, we curiously see no significant areas of increased IWV in the Top AR composite relative to all AR events. For vIVT, we only observe a small area of significantly greater anomalies in Top AR compared to AR composite (Fig. 3b), partially reflective of a poleward extension of moisture anomalies in Top AR timesteps relative to all ARs (Fig. 3a) as well as stronger pressure gradients near the coast (Fig. 3c). This investigation of moisture and moisture transport reveals surprisingly little difference between Top AR and AR environments, suggesting that column-integrated moisture availability may not be a discriminator for the highest-precipitation Antarctic AR timesteps. Instead, higher intensity precipitation in Top AR timesteps may result from a more efficient conversion of moisture into precipitation via lift (Fig. 2c) and a favorable thermodynamic environment.

We continue an investigation of moisture within AR environments with a plot of surface latent heat flux (Fig. 3c) to explore surface evaporation anomalies in the vicinity of ARs and Top ARs. We observe that AR environments feature significantly more anomalous evaporation east, west, and equatorward of the AR center. Anomalous near-surface geostrophic flow subsequently enables the transport of this evaporated moisture into the AR (Fig. 3c SLP anomaly). Compared to all AR environments, Top AR environments do not feature elevated anomalous evaporation within the anomalous near-surface geostrophic flow capable of transporting evaporated moisture into the AR. However, zooming out in time and space, we observe significantly more evaporation in the AR, and subsequently Top AR group, west of the AR and at lower latitudes (30°S) in the days prior to AR landfall (Supplementary Fig. 1). This lower latitude anomalous evaporation may represent a moisture source for landfalling precipitation, consistent with an East Antarctic case study²⁷, but a moisture tracking analysis performed for a case study or at a regional scale is necessary to verify this assertion. We conclude that during landfall, ARs likely source some moisture from areas east and west of the AR at latitudes equatorward of 40°S, but given the similarities in IWV and vIVT between AR and Top AR environments, this moisture source does not appear responsible for the difference in precipitation intensity between these two categories.

The above results highlight significant differences between AR and Analog environments including (1) more precipitation, (2) higher

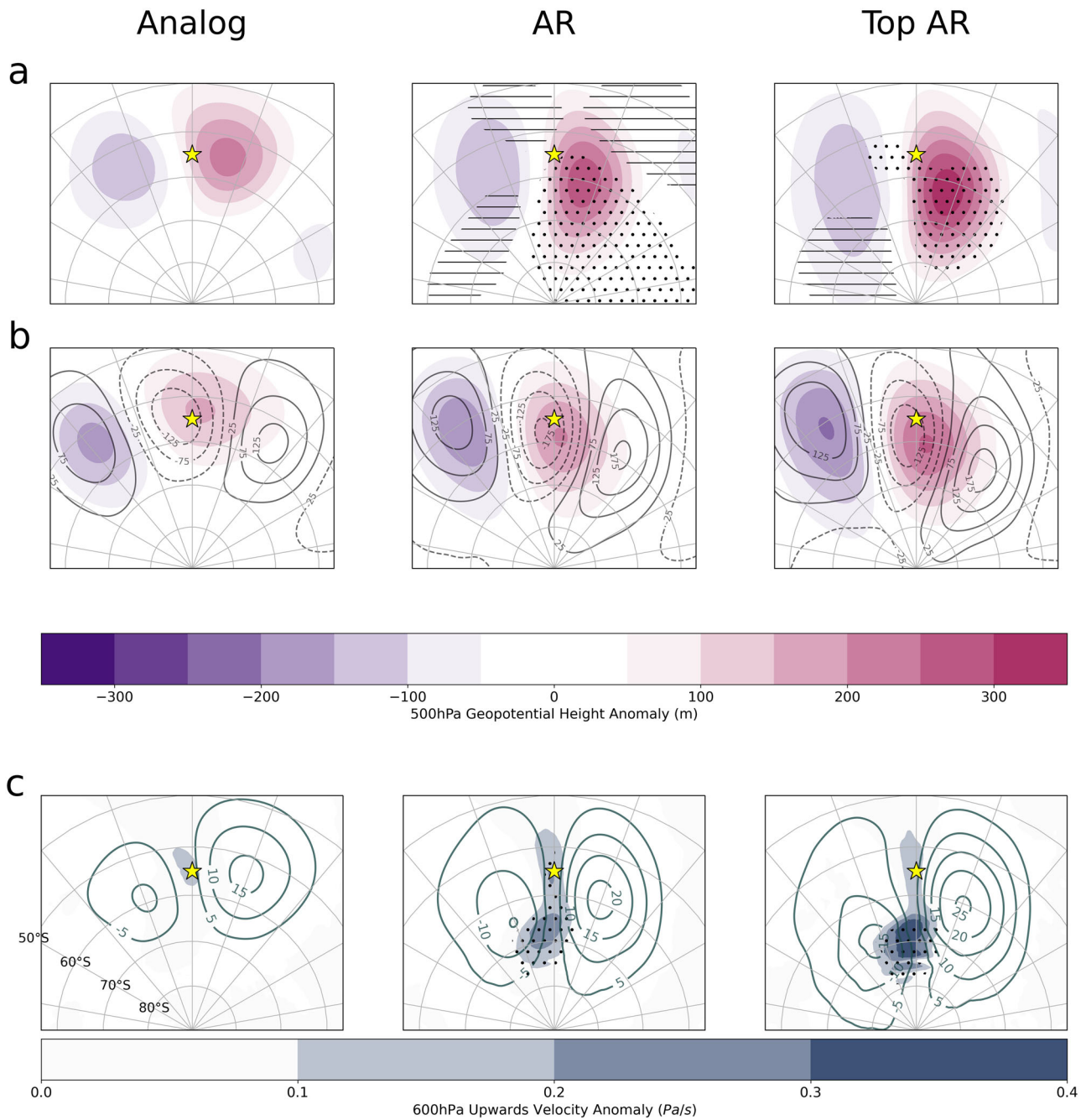


Fig. 2 | AR synoptic-scale dynamics. Composites for Analog, AR, and Top AR timesteps from 90°S to 40°S centered on the AR center at 55°S (yellow star). **a** H500 anomalies at the time of AR landfall (pink and purple shading) with stippling (hatching) where there is a significantly higher (lower) value in the AR group relative to the Analog group or in the Top AR group relative to AR group. Significance is only considered at grid points where the difference in composite height anomalies is greater than 25 m. **b** H500 anomalies 24 hours before the time of AR landfall (pink and purple shading) and the change in H500 anomalies over 48 hours (24 h after AR landfall minus 24 h before AR landfall) (black contours in m). **c** SLP anomalies (dark green contours in hPa) and 600-hPa upward vertical motion (blue shading) with stippling where there are significantly higher values in the AR group relative to the Analog group or in the Top AR group relative to the AR group. Significance is only considered at grid points where the difference in composite upward vertical motion exhibits a magnitude greater than 0.05 Pa/s.

near-surface temperature anomalies, (3) a higher-amplitude and poleward-shifted flow pattern in the middle troposphere (4) stronger atmospheric vertical motion near the coast, (5) elevated levels of anomalous moisture and meridional moisture transport, and (6) higher levels of anomalous evaporation upstream of the AR. When comparing the subset of Top AR timesteps to all AR environments, we observe significant differences in the impacts and dynamics listed above but, surprisingly, we do not observe physically meaningful differences in the moisture accompanying the ARs. Together, these results indicate that the amplitude of the mid-troposphere

flow pattern and lifting mechanisms associated with the AR's attendant cyclone play a significant role in distinguishing Top AR timesteps from all ARs. The apparent importance of synoptic-scale dynamics in differentiating Top ARs from ARs motivates further investigation into planetary-scale atmospheric dynamics associated with the three categories of timesteps.

Planetary-scale AR environments

To understand the factors that establish the synoptic-scale environments conducive to ARs and Top ARs, we examine the interaction between

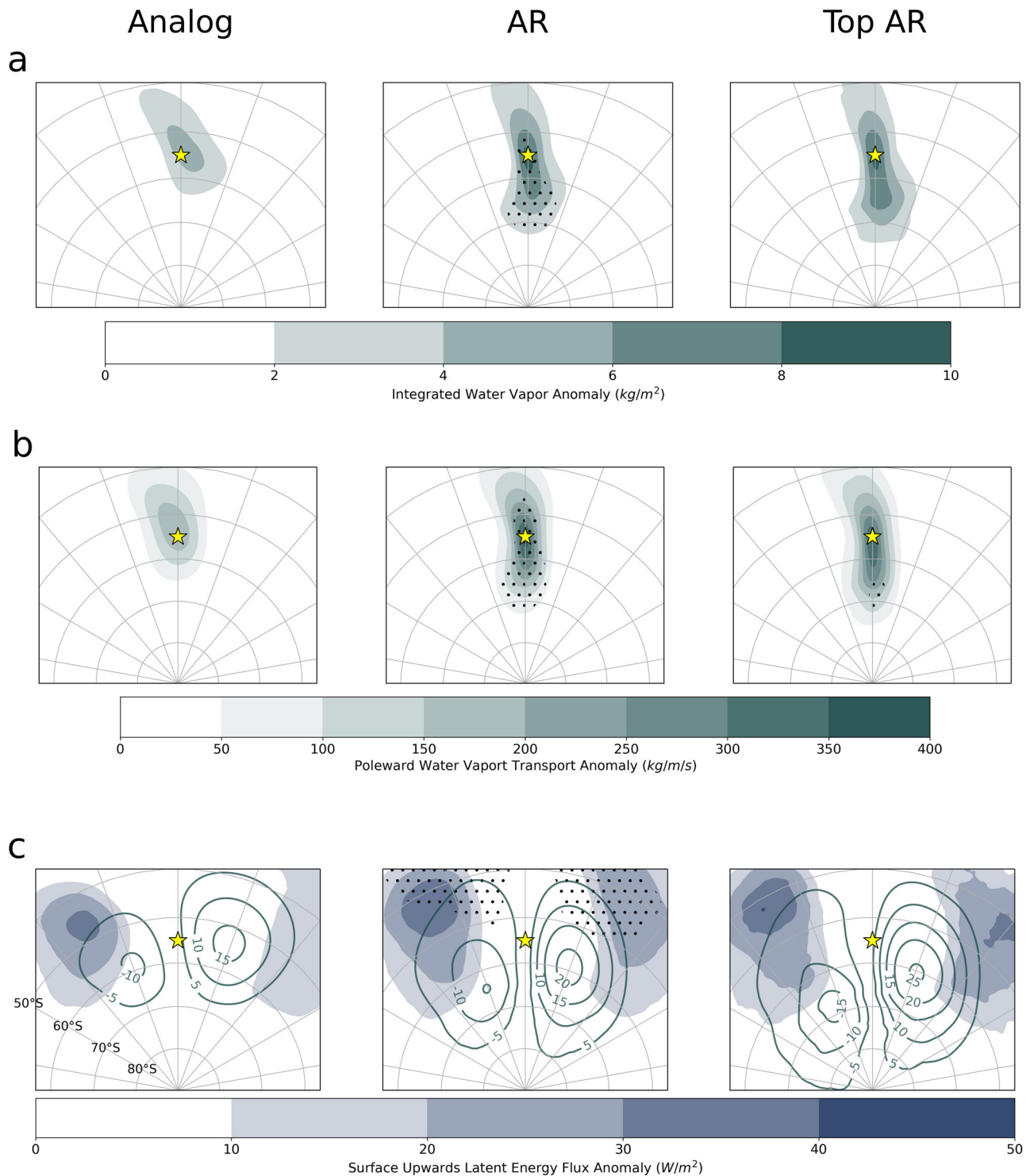


Fig. 3 | AR moisture. Composites for Analog, AR, and Top AR timesteps from 90°S to 40°S centered on the AR center at 55°S (yellow star). **a** IWV anomalies (green shading) with stippling where there are significantly higher values in the AR group relative to the Analog group or in the Top AR group relative to the AR group. Significance is only considered at grid points where the difference in composite IWV is greater than 2 kg/m². **b** vIVT anomalies (green shading) with stippling where there are significantly higher values in the AR group relative to the Analog group or in the

Top AR group relative to the AR group. Significance is only considered at grid points where the difference in composite vIVT is greater than 50 kg/m/s. **c** Surface upwards latent energy flux anomalies (blue shading) with stippling where there are significantly higher values in the AR group relative to the Analog group (middle) or in the Top AR group relative to the AR group (right) at grid points where the difference in anomalies is greater than 10 W/m². SLP anomalies are shown in dark green contours in hPa.

midlatitude and tropical dynamics prior to the development of Antarctic ARs. Due to the longitudinally asymmetric nature of tropical convection²⁸, we perform a regional analysis by splitting the AIS into West (e.g. Marie Byrd Land and the Antarctic Peninsula), East 1 (e.g. Dronning Maud Land

and Enderby Land), and East 2 (e.g. Wilkes Land, Adélie Land, and Ross Ice Shelf) sectors (Fig. 1b). We then compare differences in the percentage of timesteps that feature deep tropical convection 4 days before Analog, AR, and Top AR timesteps for each sector. Additionally, we plot composites of

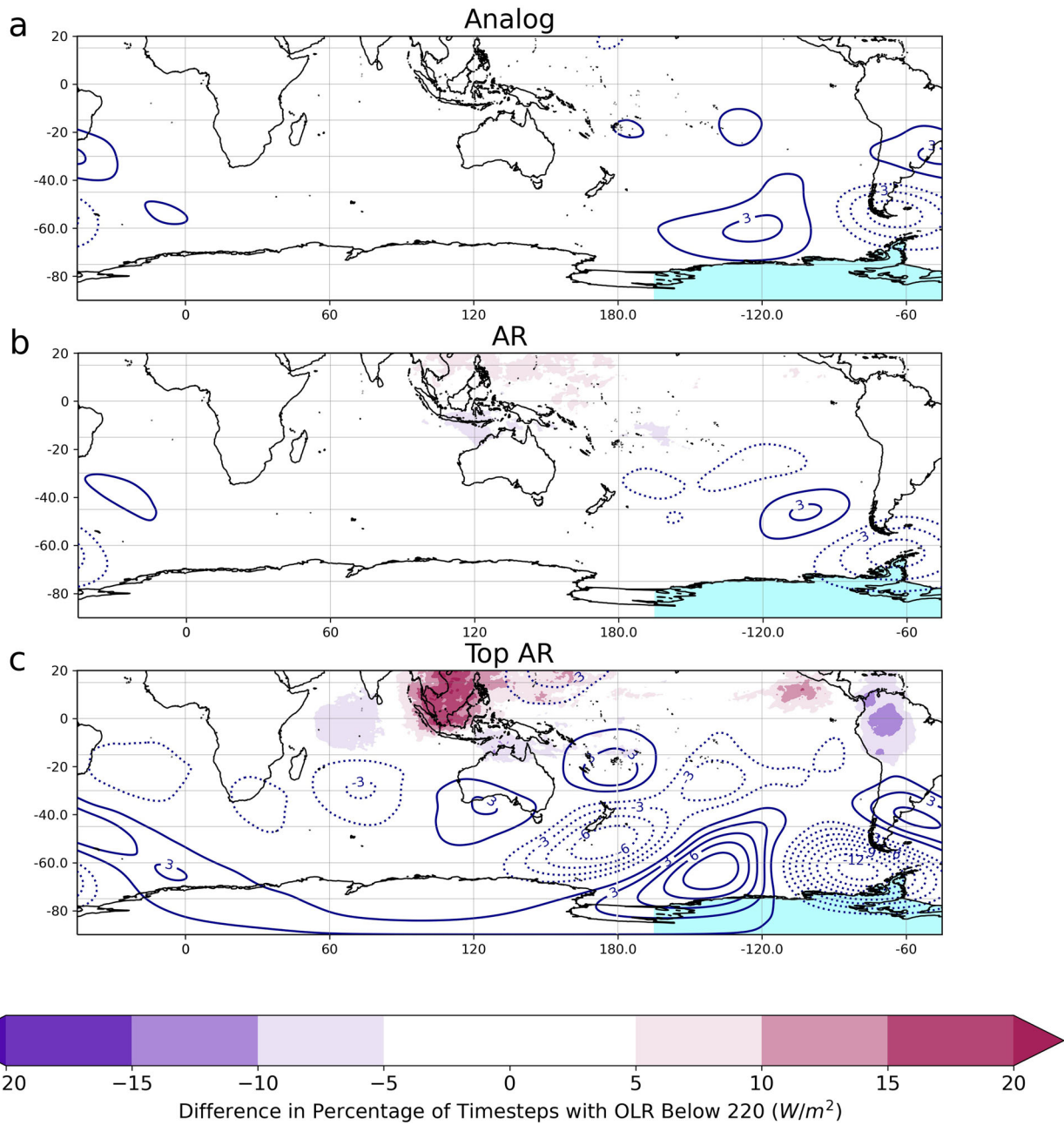


Fig. 4 | West sector AR planetary-scale dynamics. West sector longitudes (light blue shading). 200-hPa streamfunction anomaly composites in $10^6 \text{ m}^2/\text{s}$ for (a) Analog, (b) AR, and (c) top AR timesteps averaged over the four-day period prior to AR landfall (dark blue contours). Statistically significant differences in the percentage of timesteps with outgoing longwave radiation below 220 W/m^2 from 20°S to 20°N between (b) AR and Analog timesteps, (c) Top AR and AR timesteps (purple and pink shading) four days prior to AR landfall.

streamfunction anomalies during the 4-day period preceding each timestep to identify the existence of Rossby waves excited by tropical convection that may influence AR development within each sector.

In the West sector, we observe anomalous anticyclonic flow at upper-levels over the Drake Passage in both the Analog and AR streamfunction composites with anomalous cyclonic flow directly west of the Drake Passage in the Analog composite and northwest of the Drake Passage in the AR composite, but no consistent connection to Rossby wave trains emanating from middle or tropical latitudes (Fig. 4a, b). However, the West sector Top AR composite features a statistically significant (not shown) wave train stretching from the east Indian Ocean to West Antarctica (Fig. 4c). We also observe significantly elevated tropical convection (pink shading) over Indonesia 4 days before Top AR landfalls in the West sector. We conclude

that the high-amplitude flow pattern that characterizes West sector Top AR environments is frequently associated with a Rossby wave train that can be reinforced by anomalous tropical convection in the East Indian Ocean.

We also observe some differences between the cold (MJJAS) and warm (DJFM) seasons with respect to West sector Top ARs, noting these seasons have different subtropical and midlatitude jet configurations which serve as Rossby wave sources and wave guides. Warm season Top AR environments feature anomalous convection primarily in the south central Pacific that interacts with a midlatitude wave train to produce the high-amplitude flow pattern observed in the vicinity of Top ARs (Supplementary Fig. 2b). On the other hand, cold season West sector Top AR environments are associated with anomalous tropical convection over Indonesia and a Rossby wave train stretching from Australia to West Antarctica (Supplementary Fig. 2c).

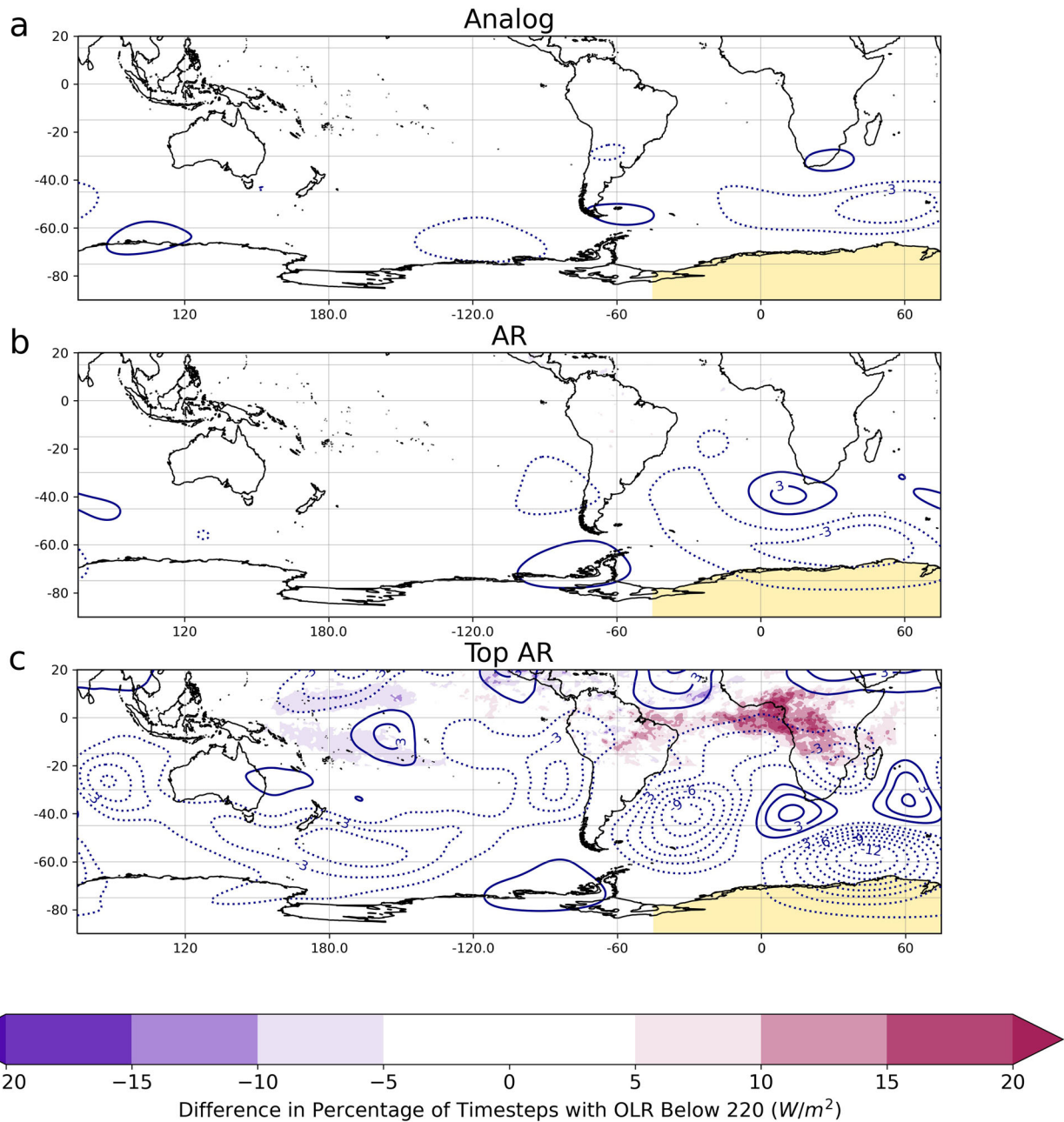


Fig. 5 | East 1 sector AR planetary-scale dynamics. East 1 sector longitudes (yellow shading). 200-hPa streamfunction anomaly composites in $10^6 \text{ m}^2/\text{s}$ for (a) analog, (b) AR, and (c) top AR timesteps averaged over the four-day period prior to AR landfall (dark blue contours). Statistically significant differences in the percentage of timesteps with outgoing longwave radiation below 220 W/m^2 from 20°S to 20°N between (b) AR and Analog timesteps, (c) top AR and AR timesteps (purple and pink shading) four days prior to AR landfall.

We conclude that in the West sector, Top AR environments are associated with low and mid-latitude wave trains that can be augmented by tropical convection, and that the tropical source region for these wave trains can vary as a function of season.

Similar to the West sector, we observe no significant connections to low or mid-latitudes for the Analog and AR timesteps within the East 1 sector. Instead, we note evidence of a weak Rex block²⁹ in both the AR and Analog composites south of Africa (Fig. 5a, b). In the East 1 Top AR composite, we observe statistically significant (not shown) dynamical linkages on the planetary-scale. Namely, tropical convection over tropical South America and an attendant anticyclonic maximum interacts with an existing wave pattern to intensify anomalous cyclonic flow southwest of South Africa. Concurrently, anomalous convection over the Democratic Republic of

Congo intensifies an anticyclonic maximum over Mozambique (Supplementary Fig. 3), resulting in a strong Omega block off the coast of the East 1 region (Fig. 5c). Seasonal variations in this setup include a spatial shift of anomalous tropical convection towards southern Africa (20°S to 30°S) during the warm season, associated with the southern shift of the ITCZ (Supplementary Fig. 4b), and towards the west over the southern Atlantic during the cold season (Supplementary Fig. 4c). As a result, the anticyclonic flow over Mozambique is much weaker, the anomalous cyclonic flow is not split into two distinct maxima, and the block near East 1 region resembles more of a Rex-block in the cold season. We conclude that East 1 Top ARs are driven by the propagation of midlatitude Rossby waves that interact with anomalous anticyclonic flow anomalies accompanying tropical convection over Africa and South America. Similar to the West sector, these

teleconnections vary seasonally and are unique to the Top AR environments since they are not present in the AR or Analog composites.

In the East 2 sector, we do not observe a strong connection to mid or low-latitudes for the Analog, AR, or Top AR categories. However, we do observe a blocking pattern associated with Top AR environments that is not present in AR or Analog environments (Supplementary Fig. 5). The setup of this blocking pattern is seasonally dependent, with cold season Top AR environments featuring a stronger blocking high compared to warm season Top AR environments (Supplementary Fig. 6).

Discussion

In this study, we identify landfalling AR timesteps around Antarctica from 1980 to 2019, an Analog collection (timesteps most similar to the synoptic-scale environments that characterize ARs but are not associated with an AR) and a Top AR collection (a subset of AR timesteps that rank in the top 10% in terms of snowfall intensity). This study extends prior regional and case study research on Antarctic ARs by comparing these three categories and their associated dynamical and thermodynamic environments across the entirety of Antarctica. Through this work, we identify discriminators for the full collection of AR environments and for a subset of Top AR environments.

Our circumpolar results identifying discriminators of Antarctic AR environments support and generalize existing regional and case study literature. Despite creating a catalog of Analog timesteps that most closely match the synoptic-scale environments associated with AR timesteps, we find a stronger, meridionally elongated, and poleward-shifted H500 anomaly couplet during AR timesteps^{2,16,17} (Fig. 2a). This amplified mid-tropospheric flow is conducive to surface cyclogenesis (Fig. 2c) and a poleward flux of warm moist air¹⁰ towards Antarctica (Fig. 1c, 3a). As exemplified by past case studies^{6,16,27}, lower-tropospheric warm-air advection along with latent heat release near the coast can amplify the mid-tropospheric ridge downstream of an AR (Fig. 2b), which is conducive to the development of a blocking pattern (Figs. 4b, 5b). This all can prolong AR impacts by slowing the prevailing westerly flow at upper-levels.

In addition to anomalous moisture in the footprint of the AR (Fig. 3a, b), we identify a possible AR moisture source in the form of anomalous evaporation upstream of the AR between 40°S to 50°S (Fig. 3c) and behind the cyclone's cold front (Fig. 1c). This circumpolar signal is consistent with existing literature. For instance, Terpstra et al.²⁷ located the dominant moisture source of one East Antarctic AR around 40°S, Sodeman and Stohl³⁰ identified average source regions for Antarctic moisture between 46°S–50°S, and Dacre et al.³¹ found that precipitation attributable to an AR's attendant cyclone is sensitive to the amount of moisture in the antecedent environment east of a developing cyclone that can be lifted via the cyclone's warm conveyor belt.

Near the coast, an Antarctic AR's attendant cyclone drives anomalous vertical motion (Fig. 2c), via a combination of orographic lift and dynamical lift associated with the warm conveyor belt¹⁷, resulting in anomalous precipitation (Fig. 1a)^{14,32}. Along with precipitation, the dynamics and thermodynamics of AR environments result in warm near-surface temperatures (Fig. 1c) driven by increased downward longwave radiation from cloud cover and warm-air advection^{7,10,16,33,34}.

We find that Top AR environments are uniquely influenced by anomalous tropical convection that initiates or enhances midlatitude Rossby waves and subsequent landfalling Antarctic ARs. However, these planetary-scale Top AR drivers vary by season and region, possibly due to seasonal variations in the subtropical and midlatitude jets, as well as Rossby wave sources including anomalous tropical convection.

Top AR environments in the West sector feature Rossby wave trains sourced from two distinct areas of enhanced convection, one over Indonesia and one over the western south Pacific that result in a high latitude ridge at ~180°W and a midlatitude ridge at ~130°W, respectively. This pattern is consistent with previous case studies^{19,35,36} and Clem et al.¹⁹, who found a strong correlation between deep convection in the south-central tropical Pacific and warm season extreme ARs over the Antarctic Peninsula and

Bellingshausen Sea. Tropical teleconnections to West Antarctica are generally rare during austral summer due to weaker Rossby wave sources in the tropics and a strong polar jet that inhibits Rossby Wave propagation towards high latitudes^{37,38}, which may explain the larger fraction of west Top AR timesteps in the cold season compared to the warm season. For cold season Top ARs in the west sector, we observe a muted stream function anomaly pattern, including reduced tropical convection in the South Pacific that aligns with a northward shift of the Inter Tropical Convergence Zone (ITCZ) during these months.

The association of East 1 Top ARs with tropical convection over eastern South America, and a resulting Omega block near Dronning Maud Land (Fig. 5), generalizes previous case study work in this region associating extreme weather with blocking highs^{34,39–41} that develop in conjunction with the downstream propagation of Rossby waves⁴⁰. Shields et al. examined the relationship between ARs and large-scale modes of variability (e.g. SAM, PSA2, and PDO) and found that a positive Indian Ocean Dipole (IOD) during El Niño is significantly correlated with AR precipitation in eastern Dronning Maud Land (our East 1 region)⁴². The IOD positive phase features warmer SSTs in the western Indian Ocean and is correlated with more convection over central equatorial Africa⁴³ as well as subsidence over Australia and New Zealand⁴⁴, consistent with our East 1 Top AR composite (Fig. 5c).

East 2 Top AR environments also feature a blocking high but, unlike the West and East 1 regions, they do not feature evidence of Rossby waves sourced from the tropics. The East 2 region experiences more blocking highs compared to the other two regions, however, due to the presence of a climatological split in the westerly jet in that location^{19,45}. This relationship may also explain the larger percentage of Top AR timesteps in East 2 compared to East 1 (Fig. 1b). The association of a blocking setup with East 2 Top AR timesteps further supports existing research associating blocking highs with ARs¹⁶ and extreme precipitation events on the AIS^{46,47}.

Although planetary-scale dynamics associated with Top ARs vary by region, all three regions feature precipitation-enhancing local anomalies relative to all AR timesteps. Specifically, a higher amplitude mid-tropospheric wave (Fig. 2a) promotes stronger cyclogenesis (Fig. 2c) and thus enhanced vertical motion near the Antarctic coast compared to all ARs (Fig. 2c). Vertical motion allows for condensation and deposition of water vapor, resulting in precipitation over the continent. Besides cyclogenesis¹⁷, enhanced vertical motion during Top AR timesteps compared to all ARs can be further modulated by an AR's orientation relative to the coast, the presence of barrier jets^{48,49}, or a near-surface cold dome over the continent⁵⁰. These phenomena are more appropriately studied at a regional or case study scale, and the relative importance of the aforementioned lifting mechanisms that contribute to Antarctic AR precipitation remains an open question.

The enhancement of synoptic-scale anomalies in Top AR compared to AR environments results in elevated temperature anomalies (Fig. 1c) and more precipitation over the AIS (Fig. 1a). However, similar to the regional analysis from Baiman et al.¹⁷, Top AR synoptic-scale environments do not feature meaningful differences in IWV, vIWT, or evaporation anomalies (Fig. 3a, b) relative to all AR timesteps, suggesting that synoptic-scale dynamics and the resultant lift play a more important role than moisture availability in driving AR precipitation intensity at short time scales. This is further supported by the disproportionate number of Top AR timesteps in austral fall and winter, when the atmosphere is drier but the amplitude of the circulation is higher. Other factors possibly driving AR precipitation intensity that are outside of the scope of this study include but are not limited to the vertical distribution of moisture in an AR²⁷, the angle between the AR and the coast⁵¹, the development of barrier jets that can cause AR moisture to precipitate before reaching the continent^{17,48,49}, cloud microphysical properties that influence the efficiency of snow growth, and the variability in local-scale orography⁵². While further research is necessary to rank the relative importance of all precipitation drivers to Antarctic AR precipitation, our finding that synoptic-scale dynamics are more important than vertically integrated moisture in determining Antarctic AR precipitation intensity on

short time scales challenges the identification of extreme ARs based solely on IWV or vIVT anomalies^{13,19,25}.

For this study we define high-impact ARs by snowfall intensity, as this is the dominant AR impact on the AIS in the current climate^{2,14}. We highlight the relative importance of synoptic-scale dynamics over moisture availability in dictating AR precipitation impacts, and we identify planetary-scale patterns that support high-impact ARs in the current climate. In order to explore the utility of these planetary-scale patterns for predicting land-falling Antarctic ARs, we briefly investigate the correlation between all 4-day streamfunction anomalies during 1980–2019 and the regional Top AR streamfunction composites shown in Figs. 4c and 5c. As the correlation between an arbitrary streamfunction pattern and a Top AR streamfunction composite increases, the likelihood of an Antarctic AR in that region increases (Supplementary Figs. 7b and 8b). However, a high correlation with the Top AR streamfunction composite (Figs. 4c and 5c) is not a sufficient predictor for an Antarctic AR (Supplementary Figs. 7 and 8). In other words, a streamfunction composite conducive to an Antarctic AR is not always associated with an Antarctic AR and vice versa.

In addition to further research that considers the planetary-scale environment as one of the multiscale predictors of Antarctic ARs, environmental drivers of high-impact ARs identified in this study should also be leveraged to examine ARs in future climates. We find that although anomalous moisture is a vital component of high-impact ARs (Fig. 3a), moisture transport and availability at the time of AR landfall is not a discriminator of high-impact ARs relative to the full distribution of ARs, implying that AR impacts may not scale proportionally with a warmer and more moist climate. By observing little difference in local moisture transport anomalies between ARs and Top ARs, which is the main variable used for AR detection, we can begin to dissociate AR impacts from the AR detection scheme and potentially focus on AR metrics that feature a more direct link to impacts. Just as there is value in measuring tropical cyclone dynamics and impacts beyond the variables that define their intensity (i.e., wind speed or mean sea-level pressure), there might be value in analyzing AR dynamics using impact-based metrics as opposed to the variables that commonly define the presence of an AR (i.e., IVT and IWV)⁵³. As Antarctic AR research inevitably turns to future AR impacts and the community reckons with AR detection in an increasingly moist atmosphere, we submit the importance and the potential utility of larger-scale dynamics in the detection and analysis of ARs.

Methods

Data and AR detection

This study uses Modern-Era Retrospective Analysis for Research Applications, version 2 (MERRA-2) reanalysis data¹⁸ between 1980–2019 with a latitude-longitude grid spacing of 0.5° x 0.625°. We define the Antarctic Ice Sheet and Ice Shelves in MERRA-2 based on masks from Zwally et al.⁵⁴ that are available through the Ice Sheet Mass Balance Intercomparison Exercise. We apply a polar-specific AR detection algorithm developed by Wille et al.¹⁰ to identify landfalling Antarctic ARs within MERRA-2 data. An advantage of this algorithm compared to global AR detection algorithms is that it is calibrated for the colder, drier environments that characterize Antarctic ARs³². We note that this algorithm has a relatively high moisture threshold for AR detection compared to other methods, which means the ARs observed in this study are more likely to be high-impact events²⁶. We choose a version of the Wille et al.¹⁰ detection algorithm based on meridional vapor transport (vIVT), which better captures dynamically-driven AR precipitation compared to an algorithm based on integrated water vapor (IWV)². This detection algorithm identifies ARs based on two requirements: an area (1) where the vIVT ranks above the 98th percentile relative to a monthly climatology between 1980–2019 and (2) that extends at least 20° in latitude². ARs are identified over the Antarctic ice sheet or ice shelves in 17,418 MERRA-2 3-hourly timesteps.

In order to obtain a broad circumpolar view of AR drivers, we do not consider how ARs evolve during their lifetime. Instead, we analyze individual 3-hourly timesteps in which ARs make landfall over the Antarctic Ice

Sheet or Ice Shelves. Maclennan et al.¹⁴ found that the intensity of precipitation over the continent decreases after an AR makes landfall, indicating that individual landfalling timesteps capture the highest intensity precipitation associated with AR events.

Defining Analog, AR, and Top AR timesteps

To examine the environments associated with landfalling ARs, we use a 500-hPa geopotential height anomaly (H500) curve at 55°S (e.g. Supplementary Fig. 9b) as a proxy for the synoptic-scale environment associated with an AR timestep. We use 500-hPa geopotential height to define AR environments in order to target mid-tropospheric flow patterns that favor surface cyclogenesis and subsequent AR development. In particular, we use 6-hourly H500 anomalies that are linearly interpolated to 3-hourly resolution to match the temporal resolution of the AR detection algorithm. 55°S is chosen as a proxy latitude for AR environments because it represents the average latitude of maximum climatological H500 variability around Antarctica (Supplementary Fig. 9a). For every AR that overlaps with the ice sheet or ice shelves between 1980–2019, we position an 80° longitude window on the AR center and isolate the H500 anomalies along 55°S within that window, producing a H500 anomaly curve as in Supplementary Fig. 9b. For 92% of the landfalling ARs, we identify the AR center at 55°S by searching for the position of the AR within a latitude band between 53–57°S. The remaining 8% of landfalling ARs are not detected within 53–57°S, so we calculate the AR center at 55°S using a wider latitude band between 45–65°S. This methodology results in a collection of 17,418 H500 anomaly curves that represent the synoptic-scale environments associated with landfalling Antarctic ARs (e.g. Supplementary Fig. 9b).

Next, we create a catalog of no-AR timesteps by starting with all H500 anomaly timesteps between 1980–2019 and removing an 80° longitude window centered on each AR detected poleward of 53°S. We also remove +/- 2 days of data within that same longitude window centered on the detected AR to remove any synoptic-scale environments that accompany a detected AR. We are left with a collection of H500 anomaly timesteps between 1980–2019 that are not associated with an Antarctic AR. Finally, we construct an Analog collection of H500 anomaly curves, which are defined as those H500 anomaly curves that most closely resemble the H500 anomaly curves associated with each landfalling Antarctic AR. In particular, we search the no-AR catalog within the same longitude window used for each detected AR for the H500 anomaly curve at 55°S that has the closest Euclidean distance to the H500 anomaly curve associated with each AR. The Analog collection exhibits strong similarity to the synoptic-scale environments accompanying the AR timesteps based on visual inspection (e.g. Supplementary Fig. 9b) and a statistical correlation analysis. Namely, 99% of the AR curves are positively correlated with their corresponding Analog curves, and 83% of AR curves have a Pearson correlation coefficient greater than 0.5.

Although ARs can be associated with surface melt events and rain^{10,20,21} and their mesoscale surface impacts can be modulated by sublimation during foehn events⁵⁵ and firm processes, they primarily impact the AIS via snowfall in the current climate¹⁴. We choose MERRA-2 snowfall intensity over other reanalysis products because MERRA-2 accumulated precipitation (precipitation - sublimation) over Antarctica is shown to most closely represent ice core-derived accumulation⁵⁶. To attribute snowfall rate to each AR timestep, we calculate the total snowfall over the ice sheet and ice shelves from MERRA-2 within an 80° longitude window centered on each landfalling AR in Gt/hr. We then repeat this calculation for each Analog timestep to determine the snowfall rate associated with each Analog timestep (Fig. 1a). We tested the sensitivity of snowfall rates to the size of the aforementioned longitude window and found that the amount of AR-related snowfall increases as the longitude window is extended to a size of 80°, but then plateaus for larger windows. We name the subset of 1742 AR timesteps associated with the most snowfall, “Top ARs”, which are those timesteps that rank in the top 10% of AR timesteps in terms of snowfall intensity, following the example of previous extreme precipitation studies^{22,57,58}. Note that we only use snowfall to determine the Top AR

timesteps since it is the predominant precipitation type in Antarctica, but our results are not sensitive to this choice. Selecting the Top AR category using total precipitation (snow+rain) results in a Top AR collection that features 99% of the same timesteps, meaning that the Top ARs represent AR timesteps with the most total precipitation as well as total snowfall. The three collections of timesteps derived in this section (Analog, AR, and a Top AR subset) are used throughout the study to identify atmospheric properties unique to AR and Top AR environments, respectively.

The Analog, AR and Top AR categories discussed above are defined based on timesteps, however, it is important to also consider how AR timesteps relate to AR events persisting over multiple timesteps. Note that this is the only paragraph of this study that addresses AR events rather than timesteps. By requiring 24 hours or 20 degree longitude separation between events, we find that the 17,418 landfalling AR timesteps cluster into 2720 AR landfalling events ranging in length from 3 to 135 hours (Supplementary Fig. 10). 90% of these AR events last less than 2 days. Top AR timesteps occur during 408 of these AR events, with 388 of those 408 events featuring timesteps that do not qualify for the Top AR subset. Thus, Top AR timesteps do not represent a unique subset of AR events but rather a subset of high-snowfall timesteps that are distributed across 408 AR events. Top AR timesteps are also more likely to occur in longer AR events (Supplementary Fig. 10). When considering the top 10% of AR events based on total event snowfall, we find that 79% of these events contain Top AR timesteps, highlighting the importance of short-term, high-intensity precipitation as a component of high-impact events. We subsequently conclude that the Top AR timesteps used in this study successfully capture the top 10% of AR events by snowfall. The timestep approach we choose for this study allows us to identify Analogs and high-impact timesteps, while also isolating the unique thermodynamic and dynamic characteristics of these environments at a 3-hourly resolution. An event-based approach can smooth important sub-synoptic scale features in the flow pattern and their subsequent impacts, which is less optimal for the purposes of this study. Additional significance testing based on AR events instead of timesteps was conducted on all AR and Top AR composites in this manuscript (not shown). These tests did not yield different conclusions.

AR-centered atmospheric variable composites

We assess differences between Analog, AR, and Top AR synoptic-scale environments by compositing a variety of atmospheric variables. All composites use MERRA-2 data, with anomalies referring to differences between 3-hourly data and 40-year (1980–2019) averaged data for each month.

IWV and vIVT are calculated from 3-hourly MERRA-2 data and are available from the Atmospheric River Tracking Method Intercomparison Project (ARTMIP)^{56,59} as tier 1 source data⁶⁰. Composites of atmospheric variables including geopotential height, temperature, wind, and omega, are performed using 3-hourly data at a single isobaric level selected from 42 levels between 1000 and 0.1 hPa. We also use single-level variables including mean sea-level pressure at a 3-hourly temporal resolution and hourly total surface latent heat energy flux resampled to a 3-hourly temporal resolution¹⁸. Composites of the variables listed above are calculated for Analog, AR, and Top AR timesteps between 40–90°S, and extend from 90° west to 90° east of each AR center at 55°S (Figs. 1c, d, 2a, b, 3a–c).

Regional atmospheric variable composites

Investigating the connection between Antarctic ARs and tropical convection necessitates a separation of Antarctic ARs into regional categories due to the longitudinally asymmetric nature of tropical convection⁶¹. We choose three geographic regions: West (165°W to 45°W), which includes Marie Byrd Land and the Antarctic Peninsula, East 1 (45°W to 75°E), which includes Dronning Maud Land and Enderby Land, and East 2 (75°E to 165°W), which includes Wilkes Land, Adélie land, and the Ross Ice Shelf (Fig. 1b). We tested the sensitivity of our results to these regional boundaries and found that the three regions described above appropriately represent the spatial variability in planetary-scale dynamics, including the distribution of

outgoing longwave radiation (OLR) anomalies in the Pacific, Atlantic, and Indian Oceans four days prior to AR landfall. The subsequent methods are applied to Analog, AR, and Top AR timesteps on a regional basis in Figs. 4, 5, and Supplementary Fig. 5. These results are further separated by season in Supplementary Figs. 2, 4, 6.

We determine OLR associated with Analog, AR, and Top AR timesteps using MERRA-2 hourly upwelling longwave radiation flux at the top of the atmosphere resampled at a 3-hourly temporal resolution. We subsequently composite OLR 4 days before each Analog, AR, and Top AR timestep, consistent with time scales used in previous case studies that explore the connection between Antarctic ARs and lower latitude dynamics^{19,27,40}. We consider OLR at latitudes between 20°N–20°S and within a longitude window that extends from the AR center to 180° west of the AR center to identify areas of tropical convection that may be physically relevant to AR development. To compare the presence of tropical convection associated with each collection of timesteps, we plot the difference in the percentage of timesteps that feature tropical convection between AR and Analog (Figs. 4b, 5b shading) and between Top AR and AR (Figs. 4c, 5c) at each grid point. We impose a conservative threshold of 220 W/m² based on previous literature that associates OLR below 240 or 220 W/m² with tropical convection^{62–64}.

We calculate the streamfunction at each timestep from 3-hourly 200-hPa winds using the ‘windsparm’ python library⁶⁵. For each AR, Analog, and Top AR timestep we take the average 200-hPa streamfunction anomalies over a 4-day period prior to each AR landfall to capture the propagation of Rossby waves into the near-AR environment and to determine whether they may be induced by tropical convection. The 4-day average 200-hPa streamfunction anomaly composites are found in Figs. 4 and 5, as well as Supplementary Figs. 2, 4, 5, and 6. In Supplementary Fig. 3, to capture the evolution of the Top AR stream function over time for the East 1 region, we calculate the percentage of timesteps with OLR below 220 W/m² and the composite stream function anomalies over the 7 day-period prior to AR landfall at 12-hour intervals. Supplementary Fig. 3 shows every-other composite from this collection.

Statistical analysis

For all composite analyses, we use Welch’s T-test for a difference in means to identify locations where the AR composite is significantly different than the Analog composite. This test is appropriate for testing the difference in two population means that have different variances or different sample sizes. We consider a location within the AR composite to be significantly different from the Analog composite if the p-value is less than .01.

We use a bootstrapping method to identify locations where the Top AR composites are significantly different from the AR composites. At each location, we create a distribution of means by resampling the AR timesteps 1000 times, each with a sample size equal to the number of Top AR timesteps. We consider a Top AR composite value to be significantly different from the AR composite value if it falls above the 99th percentile or below the 1st percentile of the bootstrapped distribution of composite means at a particular grid point.

Data availability

MERRA-2 3 hourly single level and pressure level data¹⁸ are available via the Global Modeling and Assimilation Office <https://disc.gsfc.nasa.gov/datasets/>. The Wille AR catalog¹⁰ is available as part of the ARTMIP catalogs on the NCAR CGD gateway via <https://doi.org/10.5065/D6R78D1M>. The timesteps, longitude centers, and precipitation for the AR, Analog, and Top AR collections are hosted within the University of Colorado Boulder CU Scholar archive at <https://scholar.colorado.edu/concern/datasets/jw827d12x>.

Code availability

All analysis and plots were developed in Python. All code used to in analysis and plotting is available upon request from the corresponding author.

Received: 18 August 2023; Accepted: 6 March 2024;
Published online: 14 March 2024

References

- Lenaerts, J. T. M., Medley, B., van den Broeke, M. R. & Wouters, B. Observing and modeling ice sheet surface mass balance. *Rev. Geophys.* **57**, 376–420 (2019).
- Wille, J. D. et al. Antarctic atmospheric river climatology and precipitation impacts. *J. Geophys. Res. Atmos.* **126**, e2020JD033788 (2021).
- Neiman, P. J., Ralph, F. M., Wick, G. A., Lundquist, J. D. & Dettinger, M. D. Meteorological characteristics and overland precipitation impacts of atmospheric rivers affecting the West coast of North America based on eight years of SSM/I satellite observations. *J. Hydrometeorol.* **9**, 22–47 (2008).
- Ralph, F. M. et al. Atmospheric rivers emerge as a global science and applications focus. *Bull. Am. Meteorol. Soc.* **98**, 1969–1973 (2017).
- Ralph, F. M., Dettinger, M. D., Cairns, M. M., Galarnau, T. J. & Eylander, J. Defining “Atmospheric river”: How the glossary of meteorology helped resolve a debate. *Bull. Am. Meteorol. Soc.* **99**, 837–839 (2018).
- Maclennan, M. L. et al. Climatology and surface impacts of atmospheric rivers on West Antarctica. *Cryosphere Discuss.* **2022**, 1–25 (2022).
- Adusumilli, S., Fish, M. A., Fricker, H. A. & Medley, B. Atmospheric river precipitation contributed to rapid increases in surface height of the West Antarctic ice sheet in 2019. *Geophys. Res. Lett.* **48**, e2020GL091076 (2021).
- Bennartz, R. et al. July 2012 Greenland melt extent enhanced by low-level liquid clouds. *Nature* **496**, 83–86 (2013).
- Mattingly, K. S., Mote, T. L. & Fettweis, X. Atmospheric river impacts on Greenland ice sheet surface mass balance. *J. Geophys. Res. Atmos.* **123**, 8538–8560 (2018).
- Wille, J. D. et al. West Antarctic surface melt triggered by atmospheric rivers. *Nat. Geosci.* **12**, 911–916 (2019).
- Liang, K., Wang, J., Luo, H. & Yang, Q. The role of atmospheric rivers in Antarctic sea ice variations. *Geophys. Res. Lett.* **50**, e2022GL102588 (2023).
- Francis, D. et al. Atmospheric triggers of the brunt ice shelf calving in February 2021. *J. Geophys. Res. Atmos.* **127**, e2021JD036424 (2022).
- Wille, J. D. et al. Intense atmospheric rivers can weaken ice shelf stability at the Antarctic Peninsula. *Commun. Earth Environ.* **3**, 90 (2022).
- Maclennan, M. L., Lenaerts, J. T. M., Shields, C. & Wille, J. D. Contribution of atmospheric rivers to antarctic precipitation. *Geophys. Res. Lett.* **49**, (2022).
- Clem, K. R. et al. Antarctica and the Southern Ocean. *Bull. Am. Meteorol. Soc.* **104**, S322–S365 (2023).
- Pohl, B. et al. Relationship Between Weather Regimes and Atmospheric Rivers in East Antarctica. *J. Geophys. Res. Atmos.* **126**, (2021).
- Baiman, R., Winters, A. C., Lenaerts, J. & Shields, C. A. Synoptic drivers of atmospheric river induced precipitation near Dronning Maud Land, Antarctica. *J. Geophys. Res. Atmos.* **128**, e2022JD037859 (2023).
- Gelaro, R. et al. The modern-era retrospective analysis for research and applications, version 2 (MERRA-2). *J. Clim.* **30**, 5419–5454 (2017).
- Clem, K. R., Bozkurt, D., Kennett, D., King, J. C. & Turner, J. Central tropical Pacific convection drives extreme high temperatures and surface melt on the Larsen C Ice Shelf, Antarctic Peninsula. *Nat. Commun.* **13**, 3906 (2022).
- Johnson, A., Hock, R. & Fahnestock, M. Spatial variability and regional trends of Antarctic ice shelf surface melt duration over 1979–2020 derived from passive microwave data. *J. Glaciol.* **68**, 533–546 (2022).
- Trusel, L. D., Frey, K. E., Das, S. B., Munneke, P. K. & van den Broeke, M. R. Satellite-based estimates of Antarctic surface meltwater fluxes: SATELLITE-BASED ANTARCTIC MELT FLUXES. *Geophys. Res. Lett.* **40**, 6148–6153 (2013).
- Turner, J. et al. The dominant role of extreme precipitation events in antarctic snowfall variability. *Geophys. Res. Lett.* **46**, 3502–3511 (2019).
- Grams, C. M. & Archambault, H. M. The key role of diabatic outflow in amplifying the midlatitude flow: A representative case study of weather systems surrounding western North Pacific extratropical transition. *Mon. Weather Rev.* **144**, 3847–3869 (2016).
- Neiman, P. J. et al. The Landfall and Inland Penetration of a Flood-Producing Atmospheric River in Arizona. Part I: Observed Synoptic-Scale, Orographic, and Hydrometeorological Characteristics. *J. Hydrometeorol.* **14**, 460–484 (2013).
- Ralph, F. M. et al. A scale to characterize the strength and impacts of atmospheric rivers. *Bull. Am. Meteorol. Soc.* **100**, 269–289 (2019).
- Collow, A. B. M. et al. An overview of ARTMIP’s tier 2 reanalysis intercomparison: uncertainty in the detection of atmospheric rivers and their associated precipitation. *J. Geophys. Res. Atmos.* **127**, (2022).
- Terpstra, A., Gorodetskaya, I. V. & Sodemann, H. Linking sub-tropical evaporation and extreme precipitation over East Antarctica: An atmospheric river case study. *J. Geophys. Res. Atmos.* **126**, (2021).
- Yuan, X., Kaplan, M. R. & Cane, M. A. The interconnected global climate system—a review of tropical–polar teleconnections. *J. Clim.* **31**, 5765–5792 (2018).
- Rex, D. F. Blocking action in the middle troposphere and its effect upon regional climate. *Tellus* **2**, 275–301 (1950).
- Sodemann, H. & Stohl, A. Asymmetries in the moisture origin of Antarctic precipitation. *Geophys. Res. Lett.* **36**, L22803 (2009).
- Dacre, H. F., Martínez-Alvarado, O. & Mbengue, C. O. Linking atmospheric rivers and warm conveyor belt airflows. *J. Hydrometeorol.* **20**, 1183–1196 (2019).
- Gorodetskaya, I. V. et al. The role of atmospheric rivers in anomalous snow accumulation in East Antarctica. *Geophys. Res. Lett.* **41**, 6199–6206 (2014).
- Bozkurt, D., Rondanelli, R., Marín, J. C. & Garreaud, R. Foehn event triggered by an atmospheric river underlies record-setting temperature along continental Antarctica. *J. Geophys. Res. Atmospheres* **123**, 3871–3892 (2018).
- Turner, J. et al. An extreme high temperature event in coastal east Antarctica associated with an atmospheric river and record summer downslope winds. *Geophys. Res. Lett.* **49**, (2022).
- Rondanelli, R., Hatchett, B., Rutllant, J., Bozkurt, D. & Garreaud, R. Strongest MJO on record triggers extreme atacam rainfall and warmth in Antarctica. *Geophys. Res. Lett.* **46**, 3482–3491 (2019).
- Gorodetskaya, I. V. et al. Record-high Antarctic Peninsula temperatures and surface melt in February 2022: A compound event with an intense atmospheric river. *Npj Clim. Atmospheric Sci.* **6**, 202 (2023).
- Scott Yiu, Y. Y. & Maycock, A. C. On the seasonality of the El Niño teleconnection to the Amundsen sea region. *J. Clim.* **32**, 4829–4845 (2019).
- Lee, H.-J. & Jin, E.-K. Seasonality and dynamics of atmospheric teleconnection from the tropical Indian Ocean and the western Pacific to West Antarctica. *Atmosphere* **12**, 849 (2021).
- Schlosser, E. et al. An extreme precipitation event in Dronning Maud Land, Antarctica: a case study with the Antarctic Mesoscale Prediction System: Antarctic precipitation case study. *Polar Res.* **29**, 330–344 (2010).
- Hirasawa, N., Nakamura, H. & Yamanouchi, T. Abrupt changes in meteorological conditions observed at an inland Antarctic station in association with wintertime blocking. *Geophys. Res. Lett.* **27**, 1911–1914 (2000).

41. Turner, J. et al. Extreme temperatures in the Antarctic. *J. Clim.* **34**, 2653–2668 (2021).
42. Shields, C. A., Wille, J. D., Marquardt Collow, A. B., MacIennan, M. & Gorodetskaya, I. V. Evaluating uncertainty and modes of variability for antarctic atmospheric rivers. *Geophys. Res. Lett.* **49**, (2022).
43. Jiang, Y., Zhou, L., Roundy, P. E., Hua, W. & Raghavendra, A. Increasing influence of indian ocean dipole on precipitation over central equatorial Africa. *Geophys. Res. Lett.* **48**, (2021).
44. Ashok, K., Guan, Z. & Yamagata, T. Influence of the Indian Ocean Dipole on the Australian winter rainfall: INFLUENCE OF THE INDIAN OCEAN DIPOLE. *Geophys. Res. Lett.* **30**, (2003).
45. Trenberth, K. F. & Mo, K. C. Blocking in the Southern Hemisphere. *Mon. Weather Rev.* **113**, 3–21 (1985).
46. Massom, R. A. et al. Precipitation over the interior east antarctic ice sheet related to midlatitude blocking-high activity. *J. Clim.* **17**, 1914–1928 (2004).
47. Scarchilli, C., Frezzotti, M. & Ruti, P. M. Snow precipitation at four ice core sites in East Antarctica: provenance, seasonality and blocking factors. *Clim. Dyn.* **37**, 2107–2125 (2011).
48. Bromwich, D. H. Snowfall in high southern latitudes. *Rev. Geophys.* **26**, 149–168 (1988).
49. Galewsky, J. Orographic clouds in terrain-blocked flows: An idealized modeling study. *J. Atmospheric Sci.* **65**, 3460–3478 (2008).
50. Komatsu, K. K., Alexeev, V. A., Repina, I. A. & Tachibana, Y. Poleward upgliding Siberian atmospheric rivers over sea ice heat up Arctic upper air. *Sci. Rep.* **8**, 2872 (2018).
51. Wille, J. D. et al. The Extraordinary March 2022 East Antarctica “Heat” Wave. Part I: Observations and Meteorological Drivers. *J. Clim.* **37**, 757–778 (2024).
52. Agosta, C. et al. High-resolution modelling of the Antarctic surface mass balance, application for the twentieth, twenty first and twenty second centuries. *Clim. Dyn.* **41**, 3247–3260 (2013).
53. Done, J. M., PaiMazumder, D., Towler, E. & Kishtawal, C. M. Estimating impacts of North Atlantic tropical cyclones using an index of damage potential. *Clim. Change* **146**, 561–573 (2018).
54. Zwally, H. J., Giovinetto, M. B., Beckley, M. A. & Saba, J. L. Antarctic and Greenland Drainage Systems, GSFC Cryospheric Sciences Laboratory, at. http://icesat4.gsfc.nasa.gov/cryo_data/ant_grn_drainage_systems.php (2012).
55. Gehring, J. et al. Orographic flow influence on precipitation during an atmospheric river event at Davis, Antarctica. *J. Geophys. Res. Atmos.* **127**, (2022).
56. Rutz, J. J. et al. The atmospheric river tracking method intercomparison project (ARTMIP): Quantifying uncertainties in atmospheric river climatology. *J. Geophys. Res. Atmospheres* **124**, 13777–13802 (2019).
57. Moberg, A. et al. Indices for daily temperature and precipitation extremes in Europe analyzed for the period 1901–2000. *J. Geophys. Res. Atmospheres* **111**, 2006JD007103 (2006).
58. Orłowsky, B. & Seneviratne, S. I. Global changes in extreme events: regional and seasonal dimension. *Clim. Change* **110**, 669–696 (2012).
59. Shields, C. A. et al. Atmospheric river tracking method intercomparison project (ARTMIP): Project goals and experimental design. *Geosci. Model Dev.* **11**, 2455–2474 (2018).
60. Shields C. Shields@Ucar.Edu. 3-hourly MERRA2 IVT, uIVT, vIVT, IWV data computed for ARTMIP. <https://doi.org/10.5065/D62R3QFS> (2018).
61. Kiladis, G. N. & Weickmann, K. M. Horizontal structure and seasonality of large-scale circulations associated with submonthly tropical convection. *Mon. Weather Rev.* **125**, 1997–2013 (1997).
62. Evans, J. & Webster, C. A variable sea surface temperature threshold for tropical convection. *Aust. Meteorol. Oceanogr. J.* **64**, S1–S8 (2014).
63. Mahakur, M. et al. A high-resolution outgoing longwave radiation dataset from Kalpana-1 satellite during 2004–2012. *Curr. Sci.* **105**, 1124–1133 (2013).
64. Vigaud, N., Pohl, B. & Crétat, J. Tropical-temperate interactions over southern Africa simulated by a regional climate model. *Clim. Dyn.* **39**, 2895–2916 (2012).
65. Dawson, A. Windspharm: A high-level library for global wind field computations using spherical harmonics. *J. Open Res. Softw.* **4**, 31 (2016).

Acknowledgements

ACW and RB are supported by the University of Colorado Boulder. VF and JDW acknowledge support from the Agence Nationale de la Recherche project ANR-20-CE01-0013 (ARCA). KRC acknowledges funding from the Royal Society of New Zealand Marsden Fund grant MFP-VUW2010.

Author contributions

Rebecca Baiman contributed to the conceptual direction of the work, carried out the analysis, created the figures, and drafted the manuscript. Andrew C. Winters contributed to the conceptual direction of the work, discussed results, and edited the manuscript. Benjamin Pohl contributed to the conceptual direction of the work particularly at the early stages, discussed results, and edited the manuscript. Vincent Favier, Jonathan D. Wille, and Kyle R. Clem discussed results, and edited the manuscript.

Competing interests

The authors declare no competing interests.

Additional information

Supplementary information The online version contains supplementary material available at <https://doi.org/10.1038/s43247-024-01307-9>.

Correspondence and requests for materials should be addressed to Rebecca Baiman.

Peer review information *Communications Earth & Environment* thanks Kai-Chih Tseng and the other, anonymous, reviewer(s) for their contribution to the peer review of this work. Primary Handling Editors: Min-Hui Lo, Heike Langenberg. A peer review file is available.

Reprints and permissions information is available at <http://www.nature.com/reprints>

Publisher's note Springer Nature remains neutral with regard to jurisdictional claims in published maps and institutional affiliations.

Open Access This article is licensed under a Creative Commons Attribution 4.0 International License, which permits use, sharing, adaptation, distribution and reproduction in any medium or format, as long as you give appropriate credit to the original author(s) and the source, provide a link to the Creative Commons licence, and indicate if changes were made. The images or other third party material in this article are included in the article's Creative Commons licence, unless indicated otherwise in a credit line to the material. If material is not included in the article's Creative Commons licence and your intended use is not permitted by statutory regulation or exceeds the permitted use, you will need to obtain permission directly from the copyright holder. To view a copy of this licence, visit <http://creativecommons.org/licenses/by/4.0/>.

© The Author(s) 2024